

Robustness of Neural Ratio and Posterior Estimators to Distributional Shifts for Population-Level Dark Matter Analysis in Strong Gravitational Lensing

ANDREAS FILIPP ^{1, 2, 3} YASHAR HEZAVEH ^{1, 2, 3, 4, 5, 6} AND
LAURENCE PERREAULT-LEVASSEUR ^{1, 2, 3, 4, 5, 6}

¹*Ciela Institute, Montreal Institute for Astrophysics and Machine Learning, Montreal QC, Canada*

²*Mila - Quebec AI Institute, Montreal QC, Canada*

³*Department of Physics, University of Montréal, Montréal QC, Canada*

⁴*Center for Computational Astrophysics, Flatiron Institute, New York, USA*

⁵*Perimeter Institute for Theoretical Physics, Waterloo, Canada*

⁶*Trottier Space Institute, McGill University, Montréal, Canada*

ABSTRACT

We investigate the robustness of Neural Ratio Estimators (NREs) and Neural Posterior Estimators (NPEs) to distributional shifts in the context of measuring the abundance of dark matter subhalos using strong gravitational lensing data. While these data-driven inference frameworks can be accurate on test data from the same distribution as the training sets, in real applications, it is expected that simulated training data and true observational data will differ in their distributions. We explore the behavior of a trained NRE and trained sequential NPEs to estimate the population-level parameters of dark matter subhalos from a large sample of images of strongly lensed galaxies with test data presenting distributional shifts within and beyond the bounds of the training distribution in the nuisance parameters (e.g., the background source morphology). While our results show that NREs and NPEs perform well when tested perfectly in distribution, they exhibit significant biases when confronted with slight deviations from the examples seen in the training distribution. This indicates the necessity for caution when applying NREs and NPEs to real astrophysical data, where high-dimensional underlying distributions are not perfectly known.

1. INTRODUCTION

One of the most striking open problems in modern astrophysics is that the nature of $\sim 80\%$ of the matter content of the universe is remains unknown (e.g., Davis et al. 1985; Blumenthal et al. 1984; White et al. 1987; Bertone et al. 2005). This form of matter, called dark matter, is believed to consist of new, invisible particles

that do not interact with regular matter electromagnetically. Shedding light on the nature of the dark matter particle is one of the main goals of modern cosmology and particle astrophysics (e.g., Drlica-Wagner et al. 2019).

It has been well understood that different dark matter particle properties can result in different spatial distributions of dark matter structures on various scales (e.g., Kuhlen et al. 2012). Thus, by measuring the spatial distribution of

dark matter it is possible to discriminate between different dark matter models.

The most commonly accepted dark matter model, Cold Dark Matter (CDM) has been able to explain the observations of the large scale structure (e.g., the Cosmic Microwave Background, the Baryon Acoustic Oscillations, weak lensing, etc.) with great precision and accuracy (e.g., [Hinshaw et al. 2013](#); [Planck Collaboration et al. 2020](#)). However, on subgalactic scales a number of discrepancies between the predictions of CDM and the observations of the dwarf satellites of the Milky Way have given rise to the possibility of alternative dark matter models (e.g., [Kravtsov & Borgani 2012](#)).

Strong gravitational lensing, the formation of multiple images of distant light sources due to the deflection of their light rays by the gravity of intervening structures, is a powerful probe of the subgalactic distribution of matter in the lensing galaxies and along the line-of-sight to the background sources due to its purely gravitational nature. Since different spatial distributions for the projected matter density can result in different distortions in the images, the analysis of lensed images allows the inference of these projected densities, including the abundance and distribution of subhalos. These can then be related to population-level parameters such as the halo mass function on these subgalactic scales, which are directly linked to predictions of dark matter models.

However, measuring the effect of small halos on lensed images is a challenging, nonlinear inverse problem. The signal is weak and suffers from multiple degeneracies with other nuisance parameters, such as the morphology of the background source. Furthermore, the properties of a population of dark matter subhalos correspond to a high-dimensional space (e.g., the positions and masses of a large number of subhalos), making the inference of the abundance and distribution of subhalos a difficult problem for tra-

ditional, explicit likelihood modeling methods. Past works have introduced a number of approximations in an attempt to make the problem tractable, for example by assuming Gaussian priors, linearizing the lensing model, limiting the analysis to only modeling the effect of the most massive subhalos, or performing a power-spectrum analysis (e.g., [Vegetti et al. 2010](#); [Hezaveh et al. 2016b,a](#); [Cyr-Racine et al. 2016](#); [Birrer et al. 2017](#); [Brennan et al. 2019](#); [Despali et al. 2020](#)). Despite these simplifications, these methods are still generally computationally costly, which limits the possibility of extensive testing them for potential biases.

Neural network inference frameworks, such as Neural Ratio Estimators (NREs) and Neural Posterior Estimators (NPEs), have recently emerged as a promising solution to these problems since they can be trained to approximate the intractable likelihood or the posterior of parameter distributions directly from high-dimensional input data (e.g., [Cranmer et al. 2015](#); [Baldi et al. 2016](#); [Papamakarios & Murray 2016](#); [He et al. 2016](#); [Brehmer et al. 2018](#); [Brehmer et al. 2018, 2020](#)). In principle, both analysis frameworks can marginalize over large numbers of nuisance parameters and return an optimal, unbiased likelihood or posterior for the parameters of interest. Within the context of subhalo studies with strong gravitational lensing, this means directly inferring parameters describing the population-level distribution of subhalos (e.g., the subhalo mass function) from a collection of strong lensing systems, while marginalizing over nuisance parameters, including the source galaxy morphologies, the macrolens parameters, and the parameters of an a priori unknown number of individual subhalos. Recent work has demonstrated the promise of such approaches to circumvent approximations of the intractable likelihood in strong gravitational lensing (e.g., [Brehmer et al. 2019](#); [Coogan et al. 2022](#); [Mishra-Sharma 2022](#); [Zhang et al.](#)

2022; Karchev et al. 2023; Wagner-Carena et al. 2023, 2024; Zhang et al. 2024).

Despite their potential, these methods face challenges when applied to real observational data. While these methods have been shown to work well when tested on data coming from the same distribution as the training data, their performance on out-of-distribution (OOD) data is not guaranteed. These subhalo inference frameworks rely on producing large volumes of labeled, simulated data for training, requiring a detailed match between the distributions of real and simulated data for unbiased inference. However, even using the most sophisticated simulation pipelines, it is to be expected that there will always remain some level of mismatch between synthetic and real data distributions. Given the weakness of the expected signal of interest, this leaves NPEs and NREs vulnerable to biased inference.

In this work, we investigate the performance of NREs and NPEs for the inference of the subhalo mass function in the presence of realistic distributional shifts between the training and test datasets. We produce several simulated datasets with minor variations in background source morphologies, the distribution of lens macro model parameters, subhalo profiles, and observational noise statistics and show that when the training and test datasets are distributionally shifted, the performance of the NRE and NPE can be dramatically affected. Note that these experiments are not meant to explore an exhaustive list of possible distributional shifts, but rather to establish the vulnerability of this class of methods to such shifts in strong lensing analysis.

In Section 2 we describe the simulations and the inference frameworks. In Section 3 we describe the data generation process for the inference frameworks. In Section 4, we present the details of the distributional shifts considered. In Section 5 we present the performance of the in-

ference frameworks on OOD tests and present our conclusions in Section 6. In what follows, we adopt a flat Λ CDM cosmology with parameters from Planck Collaboration et al. (2020).

2. METHODS

2.1. Bayesian Inference of Dark Matter Models

In strong lensing systems, a background source described by the parameter vector S is distorted by a mass distribution in the foreground. For example, the source could be represented as a Sérsic light profile with S containing the Sérsic parameters, or as a pixelated image with S containing the pixel values.

The foreground mass density is considered to be the sum of two components: a smooth profile for the main deflector and small-scale, local fluctuations resulting from low-mass dark matter subhalos. The smooth component is typically represented by an analytic profile, such as the Singular Isothermal Ellipsoid (SIE) profile, with L containing the parameters of this profile. Individual dark matter subhalos, m_i , are also often represented with simple analytic profiles, like the truncated Navarro-Frank-White (tNFW) profile. However, since there are a large number of these subhalos, $H = \{m_1, m_2, \dots\}$ contains these parameters for the entire subhalo population (e.g., the positions, masses, and truncation radii of a large number of subhalos). Also note that, since the number of subhalos is unknown, this is a transdimensional problem, and H could have different lengths for different models.

The parameters of individual subhalos, m_i , are drawn from a population-level distribution with parameters ϑ , which are the main parameters of interest for our studies. In principle, we are interested in the posterior distribution of these subhalo population parameters, marginalized over all nuisance parameters, S , L , H , etc. For simplicity, we collectively denote all the nui-

sance parameters as $\theta = \{S, L, H\}$ and our data as D .

To obtain the posterior distribution $p(\vartheta|\{D_i\})$ of the parameters of interest ϑ given a set of observed images $\{D_i\}$, we apply Bayes' theorem:

$$\begin{aligned} p(\vartheta|\{D_i\}) &= \frac{p(\vartheta) \prod_i p(D_i|\vartheta)}{\int d\vartheta' p(\vartheta') \prod_i p(D_i|\vartheta')} \\ &= p(\vartheta) \left[\int d\vartheta' p(\vartheta') \prod_i \frac{p(D_i|\vartheta')}{p(D_i|\vartheta)} \right]^{-1} \end{aligned} \quad (1)$$

where $p(\vartheta)$ is the prior on the population-level distribution parameters.

The models of the observations $\{D_i\}$ explicitly depend on the intermediate macro model parameters θ , which themselves depend on the population-level parameters ϑ . Thus, the likelihood $p(D_i|\vartheta)$ is the marginalization of the likelihood $p(D_i, \theta|\vartheta)$ over all intermediate model parameters θ :

$$p(D_i|\vartheta) = \int d\theta p(D_i, \theta|\vartheta) \quad (2)$$

The likelihood $p(D_i|\vartheta)$ and the posterior $p(\vartheta|\{D_i\})$ are intractable due to the high-dimensional nature of the likelihood $p(D_i, \theta|\vartheta)$, which can be expressed as:

$$\begin{aligned} p(D, \theta|\vartheta) &= p_{\text{lens}}(L) \\ &\times \text{Pois}(n_h|\bar{n}_h(\vartheta)) \prod_{i=1}^{n_h} [p_{\text{mass}}(m_{h,i}|\vartheta)p(\psi_i)] \\ &\times p_{\text{obs}}(D|\theta) \end{aligned} \quad (3)$$

with p_{lens} the likelihood of the latent lens parameters L , and $\bar{n}_h(\vartheta)$ the expected number of subhalos as a function of the parameter of interest ϑ . n_h is the realized number in a specific simulation, and $m_{h,i}$ and ψ_i are the masses and positions of the i -th subhalo in the simulated image. p_{mass} is the normalized subhalo mass function, and p_{obs} is the probability of observing

the specific image D , taking into account Poisson fluctuations and the Point Spread Function (PSF). Note that the form of the contribution of the subhalos to the likelihood assumes statistical independence between different subhalos.

Both the NRE and the SNPE effectively marginalize over the nuisance parameters by learning the intractable likelihood, enabling the posterior calculation from Equation 1.

2.2. Neural Ratio Estimator

Rather than directly learning the likelihood from the intractable integral in Equation 2 or the posterior from Equation 1, the training objective of NRE is the likelihood-to-evidence ratio $r(D, \theta|\vartheta)$:

$$r(D, \theta|\vartheta) = \frac{p(D, \theta|\vartheta)}{p_{\text{ref}}(D, \theta)} \quad (4)$$

where $p_{\text{ref}}(D, \theta)$ is the evidence, defined as the reference likelihood of an observation D occurring under any possible dark matter parameterization ϑ .

$$p_{\text{ref}}(D, \theta) = \int d\vartheta' p(\vartheta') p(D, \theta|\vartheta') \quad (5)$$

Here, $p(D, \theta|\vartheta')$ is the likelihood of an observation D given a specific set of dark matter parameters ϑ' , and $p(\vartheta')$ is the prior distribution for the dark matter parameters used in training data generation.

Predicting the likelihood-to-evidence ratio $r(D, \theta|\vartheta)$, rather than the intractable likelihood or the posterior, allows for more efficient training of the neural network. The ratio simplifies the likelihood in Equation 3 to:

$$r(D, \theta|\vartheta) = \text{Pois}(n_h|\bar{n}_h(\vartheta)) \prod_{i=1}^{n_h} [p_{\text{mass}}(m_{h,i}|\vartheta)p(\psi_i)] \quad (6)$$

because all other terms cancel out when taking the likelihood-to-evidence ratio, as they do not depend on the parameters of interest ϑ . The

ratio can be computed analytically and used as training objective, when the mass function of the dark matter subhalos is analytic, and the probability for spatial distributions is straightforward to compute, as discussed in [Brehmer et al. \(2018\)](#); [Brehmer et al. \(2018, 2019\)](#). By training the network on images D generated with different sets of parameters (θ, ϑ) and the corresponding likelihood-to-evidence ratio $r(D, \theta | \vartheta)$, the NRE learns to marginalize over the nuisance parameters θ .

The trained NRE predicts the marginal likelihood-to-evidence ratio $r(D | \vartheta)$, which can be used to calculate the posterior from Equation 1 by replacing the fraction of likelihoods with the fraction of marginal likelihood-to-evidence ratios:

$$\frac{p(D_i | \vartheta')}{p(D_i | \vartheta)} = \frac{\frac{p(D_i | \vartheta')}{p_{\text{ref}}(D_i)}}{\frac{p(D_i | \vartheta)}{p_{\text{ref}}(D_i)}} = \frac{r(D_i | \vartheta')}{r(D_i | \vartheta)} \quad (7)$$

This substitution reduces the posterior calculation to

$$p(\vartheta | \{D_i\}) = p(\vartheta) \left[\int d\vartheta' p(\vartheta') \prod_i \frac{r(D_i | \vartheta')}{r(D_i | \vartheta)} \right]^{-1} \quad (8)$$

The parameter space that needs to be integrated over is defined by the parameters of interest ϑ . For our NRE, this is a two-dimensional space (e.g., the normalization and slope of the subhalo mass function, discussed in Section 3.1), making the integral in the posterior calculation low-dimensional and tractable.

In the limit of unlimited training data from the same distribution as the test data and perfect learning, the NRE is capable of predicting the marginal likelihood-to-evidence ratio perfectly. However, in practice, these conditions are unattainable. To ensure the reliability and accuracy of the NRE at the time of inference, the trained NRE is calibrated. This calibration process addresses potential biases, overconfidence or underconfidence, and discrepancies in

the uncalibrated outputs produced by the NRE. The calibration procedure follows the method described in [Brehmer et al. \(2018, 2019\)](#).

2.3. Neural Posterior Estimator

In comparison to the NRE, the SNPE predicts the intractable posterior (Equation 1) directly. For the SNPE, a network is initially trained on a broad prior and predicts the mean with uncertainties for the parameters of interest and a number of additional parameters. The inferred posteriors on these parameters define priors to fine-tune the neural network by further training with the updated training priors.

For population inference, a set of sequential networks must be trained for each observation D_i independently. Every target image requires the training of an independent set of SNPE networks.

The distribution of the training data for the SNPE effectively serve as a prior during inference. A distributional shift between the training data and the test data can result in biased inference. However, this bias can be corrected for in the hierarchical inference procedure as described in [Wagner-Carena et al. \(2021\)](#). For this, the SNPE outputs can be incorporated into a hierarchical model to calculate the posterior of ϑ_{obs} given $\{x_{\text{obs}}\}$ following [Wagner-Carena et al. \(2023, 2024\)](#):

$$p(\vartheta_{\text{obs}} | \{D_i\}) = p(\vartheta_{\text{obs}}) \times \prod_{k=1}^{N_{\text{lens,obs}}} \frac{p(D_k | \vartheta_{\text{prior}})}{p(\{D\})} \times \prod_{k=1}^{N_{\text{lens,obs}}} \int d\theta \frac{p(\theta | \vartheta_{\text{obs}})}{p(\theta | \vartheta_{\text{prior}})} q_{\phi}(\theta | D_k, \vartheta_{\text{prior}}) \quad (9)$$

The third term represents an importance sampling integral. $N_{\text{lens,obs}}$ denotes the number of lenses and $q_{\phi}(\theta | D_k, \vartheta_{\text{prior}})$ is the posterior estimation returned by the neural network. Equation 9 re-weights the posteriors to account for the differences between the prior distribution

ϑ_{prior} and the underlying distribution in the observation ϑ_{obs} .

There is no general analytical solution to Equation 9, but the three distributions in the integral, $p(\theta|\vartheta_{\text{obs}})$, $p(\theta|\vartheta_{\text{prior}})$, and $q_\phi(\theta|D_k, \vartheta_{\text{prior}})$, are by construction Gaussian. This special configuration provides an analytical solution to the integral and allows the use of a sampling algorithm to draw from $p(\vartheta_{\text{obs}}|\{D_i\})$. We use an MCMC sampler from the `emcee` package (Foreman-Mackey et al. 2013). More details on the hierarchical inference and importance sampling can be found in Wagner-Carena et al. (2021).

3. DATA GENERATION

We test the frameworks of NRE and NPE (more specifically, Sequential NPE, SNPE) for subhalo inference using two publicly available implementations by Brehmer et al. (2019) and Wagner-Carena et al. (2024), respectively. These two models were trained on simulations with different parameterizations. Below we describe the baseline simulations (i.e. the training sets) for each model, followed by a description of the OOD test data in Section 4.

In both frameworks the individual dark matter halos are sampled from a subhalo mass function that accounts only for the subhalos in the main deflector. In this work we do not account for halos in the line-of-sight or other effects on the subhalo mass function beyond a power-law.

3.1. Training Simulations for the NRE

To simulate the lenses in the NRE framework, we use `caustics`¹ (Stone et al. 2024).

We model the light of the background source with an ensemble of 5 to 50 Sérsic profiles (Sérsic 1963), to model background sources with different complexities.

The main deflector is an elliptical power-law (EPL) profile, with the normalized surface mass

density κ

$$\kappa(x, y) = \frac{3 - \gamma_{\text{ep1}}}{2} \left(\frac{\theta_{\text{E}}}{\sqrt{qx^2 + y^2/q}} \right)^{\gamma_{\text{ep1}} - 1} \quad (10)$$

with θ_{E} the Einstein radius, γ_{ep1} the mass slope, and q the axis ratio of the mass profile. (x, y) define a Cartesian coordinate system aligned with the major and minor axis of the mass profile (Tessore & Metcalf 2015). For the case of $\gamma_{\text{ep1}} = 2.0$ the EPL profile is equivalent to an SIE profile, which we use for training data generation.

The Einstein radius θ_{E} of the EPL depends on the mass within the Einstein radius $M(\theta_{\text{E}})$

$$\theta_{\text{E}} = \sqrt{\frac{4GM(\theta_{\text{E}})}{c^2} \frac{D_{\text{ls}}}{D_1 D_s}} \quad (11)$$

and defines the typical separation scale between multiple images.

The individual dark matter halos are modeled with Navarro-Frank-White (NFW) profiles (Navarro et al. 1997). The mass of each subhalo are sampled from a mass function. The standard model of cosmology, the Λ CDM model, predicts a scale-invariant power spectrum of primordial fluctuations. From this, subhalos in galaxies are expected to follow to first order a power-law mass distribution. The power-law mass function is described by the following equation:

$$\frac{dn}{d \log m_{\text{halo}}} = \alpha \cdot M_{\text{host}} \cdot m_{\text{halo}}^\beta \quad (12)$$

with α the normalization constant of the profile, M_{host} the mass of the host galaxy, and m_{halo} the subhalo mass. To quantify and normalize the abundance of dark matter, we introduce the parameter f_{sub} , which determines the ratio of mass in the dark matter subhalos to the mass in the main deflector defined by the SIE profile

¹ <https://github.com/Ciela-Institute/caustics>

and defines the normalization α :

$$f_{\text{sub}} = \alpha \int dm_{\text{halo}} m_{\text{halo}}^{\beta+1} \quad (13)$$

$$= \frac{\int dm_{\text{halo}} m_{\text{halo}} \frac{dn}{dm_{\text{halo}}}}{M_{\text{host}}}$$

This enables efficient sampling of dark matter subhalos across different dark matter mass functions. The parameters (f_{sub}, β) define fully the dark matter population. We aim to infer these two parameters with the NRE. The prediction from Λ CDM for this power-law approximation is $f_{\text{sub}} \approx 0.05$ and $\beta \approx -0.9$ (e.g., Diemand et al. 2007; Kuhlen et al. 2007; Springel et al. 2008; Hiroshima et al. 2018).

Figure 1 shows an example of all relevant components in the simulations. From left to right, the figure displays the convergence map κ_{SIE} generated by the main deflector – an SIE profile –, the convergence map for a sample of dark matter halos κ_{NFW} , a realization of the source light, which consists of multiple Sérsic profiles, followed by the lensed image generated with the provided kappa maps and source light without PSF convolution, and finally the observation with PSF convolution and noise.

The pixel size here is 0.2 arcsec, and the PSF is assumed to be Gaussian with a full width at half maximum size of 0.87 arcsec. The noise realization in the simulation is based on the expected LSST data quality in the r-band after the full ten-year survey (Ivezić et al. 2019).

Figure 2 displays 40 randomly sampled strong lens images generated with the training data distribution from Table 1. These distributions define the training distribution. The figure illustrates the variety of the possible lens configurations that the networks learn to marginalize. The lens systems include Einstein rings, doubles, and quadruples. Such diversity is also observed and expected in real lens systems.

Table 1. The parameter distributions for the simulation of the main deflector and the source light for the training data generation of the NRE. $\mathcal{N}(\mu, \sigma)$ indicates a normal distribution with mean μ and standard deviation σ , and $\mathcal{U}[a, b]$ denotes a uniform distribution between a and b .

Parameter	Distribution
Lens galaxy	
Einstein radius θ_{E}	$\mathcal{U}[1.0, 1.5]$
Axis ratio q_{SIE}	$\mathcal{U}[0.5, 0.99]$
Orientation angle ϕ_{SIE}	$\mathcal{U}[0.0, \pi]$
Lens center $(\hat{x}_{\text{SIE}}, \hat{y}_{\text{SIE}})$	$(0, 0)$
Source light	
Number of sources N	$\mathcal{U}[5 - 50]$
Magnitude mag_{source}	$\mathcal{N}(23.5, 0.1)$
Sérsic index $n_{\text{sérsic}}$	$\mathcal{N}(2.5, 0.5) \geq 0.8$
Axis ratio $q_{\text{sérsic}}$	$\mathcal{U}[0.5, 0.99]$
Orientation angle $\phi_{\text{sérsic}}$	$\mathcal{U}[0.0, \pi]$
Sérsic radius $R_{\text{sérsic}}$	$\mathcal{N}(0.5, 0.3) \geq 0.05$
Source center $\hat{x}_{\text{source}}, \hat{y}_{\text{source}}$	$\mathcal{N}(0.0, 0.1)$

3.2. Training Simulations for the SNPE

To simulate the training data of the SNPE, we utilize the built-in strong lensing simulation code in `Platax`² by Wagner-Carena et al. (2023, 2024), which is based on `lenstronomy` (Birrer & Amara 2018; Birrer et al. 2021) and written in JAX.

The main deflector is modeled with an EPL profile, described in Equation 10. The ellipticity of the main deflector is described by two ellipticity parameters (γ_1, γ_2) given by

$$\gamma_1 = \frac{1 - q}{1 + q} \cos(2\phi) \quad (14)$$

$$\gamma_2 = \frac{1 - q}{1 + q} \sin(2\phi)$$

with q the axis ratio of the EPL profile and ϕ the angle.

² <https://github.com/swagnercarena/paltax/>

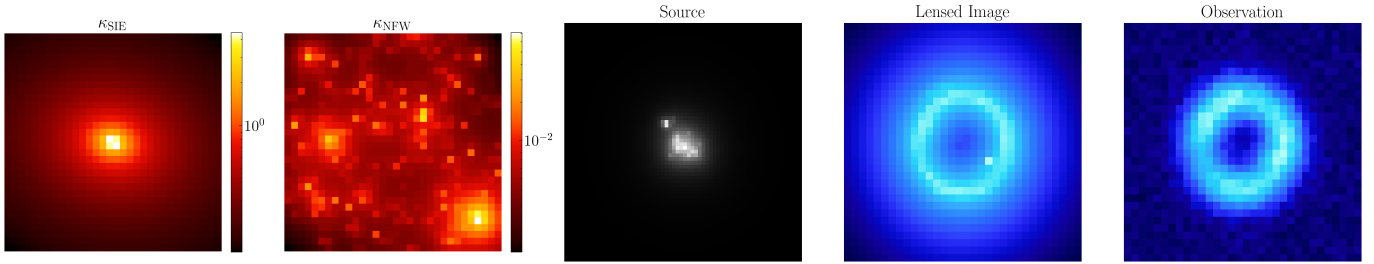


Figure 1. From the left to the right: a convergence map κ_{SIE} created with an SIE profile, the convergence map of a sample of dark matter halos κ_{NFW} , a realization of the source light, the lensed image without PSF convolution and noise, and the lensed image with PSF convolution and noise, generated with the provided kappa maps and source light.

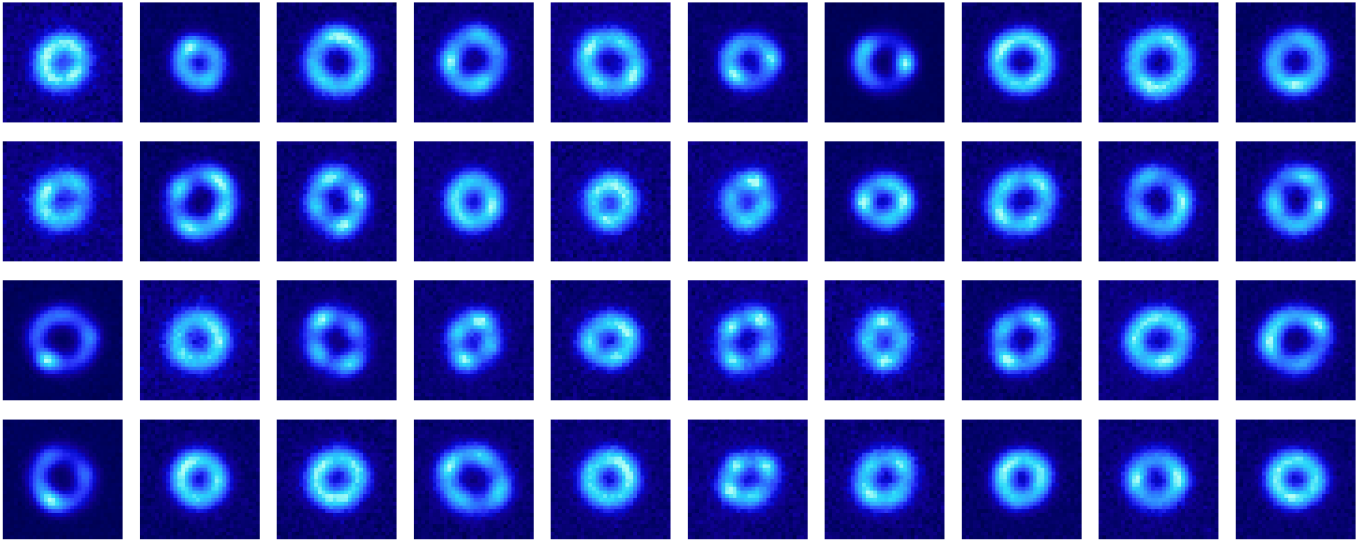


Figure 2. A sample of 40 random strong lenses, generated from the training data distribution for the NRE. The lens systems include a wide variety of closed Einstein rings, doubly imaged sources, and quadruply imaged sources. Such diversity is also seen in real observed lens systems.

In the SNPE training distribution we used tNFW profiles for the individual subhalos, which have, in comparison to the NFW profile, a finite expansion. The subhalo mass function used in the SNPE framework is the same power-law as for the NRE function, but parameterized differently:

$$\frac{d^2 N_{\text{sub}}}{dA dm_{\text{sub}}} = \Sigma_{\text{sub}} \frac{m_{\text{sub}}^{\beta}}{m_{\text{pivot,sub}}^{\beta+1}} \quad (15)$$

with Σ_{sub} the normalization of the subhalo mass function, β the mass function slope, and $m_{\text{pivot,sub}}$ the pivot mass between the minimal $m_{\text{min,sub}}$ and maximal $m_{\text{max,sub}}$ rendered subhalo

mass. In this case, the slope of the mass function is drawn from a tightly defined uniform distribution $-2.02 \leq \beta \leq -1.92$, which leaves only the normalization Σ_{sub} as a variable parameter to be inferred by the NPE.

The background sources are real pixelated galaxy images from a set of 8000 elliptical galaxies originating from the DESI survey (Dey et al. 2019), selected and compiled in Barco et al. (2024).

Figure 3 shows a sample of 40 strong lenses from the training data distribution of the SNPE. The pixel size is 0.04 arcsec and the PSF is a Gaussian PSF with a full width half maximum

Table 2. The parameter distributions for the simulation of the main deflector for the training data generation of the SNPE. $\mathcal{N}(\mu, \sigma)$ indicates a normal distribution with mean μ and standard deviation σ .

Parameter	Distribution
Einstein radius θ_E	$\mathcal{N}[1.1, 0.15]$
Mass slope γ_{EPL}	$\mathcal{N}[2.0, 0.1]$
Lens center ($\hat{x}_{\text{EPL}}, \hat{y}_{\text{EPL}}$)	$\mathcal{N}[0.0, 0.16]$
Ellipticity (γ_1, γ_2)	$\mathcal{N}[0.0, 0.1]$

size of 0.04 arcsec. The observed variety is similar to the images used to train the NRE.

The training parameter distribution is displayed in Table 2. The table shows the training parameter distributions for the main deflector, for the source images we use real images as mentioned above.

4. MISSPECIFICATION TESTS

Real observational data can have distributions that differ from those of training data. Ensuring that the network is insensitive to variations that can occur in real data is crucial for the reliability of the predictions made by machine learning models. Szegedy et al. (2013) demonstrated that even minimal, visually imperceptible variations in the input to a network can significantly alter the network’s prediction.

We test a number of small variations in the nuisance parameter distributions of the simulations. In these tests, we vary one parameter at a time, introducing variations that can be expected in real observations and may be difficult to distinguish from the assumed ground truth distributions of training data.

Our OOD and prior misspecification tests vary the following parameters:

Source Galaxies: Strong lensing magnifies sources at high redshifts. The statistical distribution of the surface brightness of these high redshift galaxies is not accurately known. The background galaxies in lensing systems are likely to be a

biased sample compared to the unlensed galaxy population at the same redshift (e.g., Hezaveh et al. 2012). Moreover, the population-level distribution of the surface brightness of background galaxies is a high-dimensional variable that is difficult to infer from large datasets of lensing systems in a hierarchical framework (although see Barco et al. 2024; Rozet et al. 2024). Therefore, it is desirable that minor modifications to this distribution do not bias the inference of dark matter model parameters. We explore this by both changing the distributions of our parametric models (composed of a number of Sérsic components) and also by using pixelated images of galaxies that exhibit different morphologies from those in the training data.

Einstein Radius: The existence of a selection bias in the Einstein radii of strong lenses is well understood (e.g., Mandelbaum et al. 2009; Collett & Cunnington 2016; Sonnenfeld et al. 2023). While we do not change the minimum and maximum Einstein radii in our training data, we modify the distribution of the test data within those bounds.

Mass Slope: The mass slope of the main deflector is known to be highly degenerate with the background source morphology (e.g., Treu et al. 2009; Schneider & Sluse 2014). In some experiments, we modify the isothermal density slope by $\sim 1\%$.

External Shear: The ellipticity of the main deflector is highly degenerate with external shear caused by the environment of the lens (e.g., Oguri et al. 2005; Koopmans et al. 2006; Sonnenfeld et al. 2013; Shu et al. 2016, 2017; Talbot et al. 2021). We introduce external shear of ~ 0.1 to

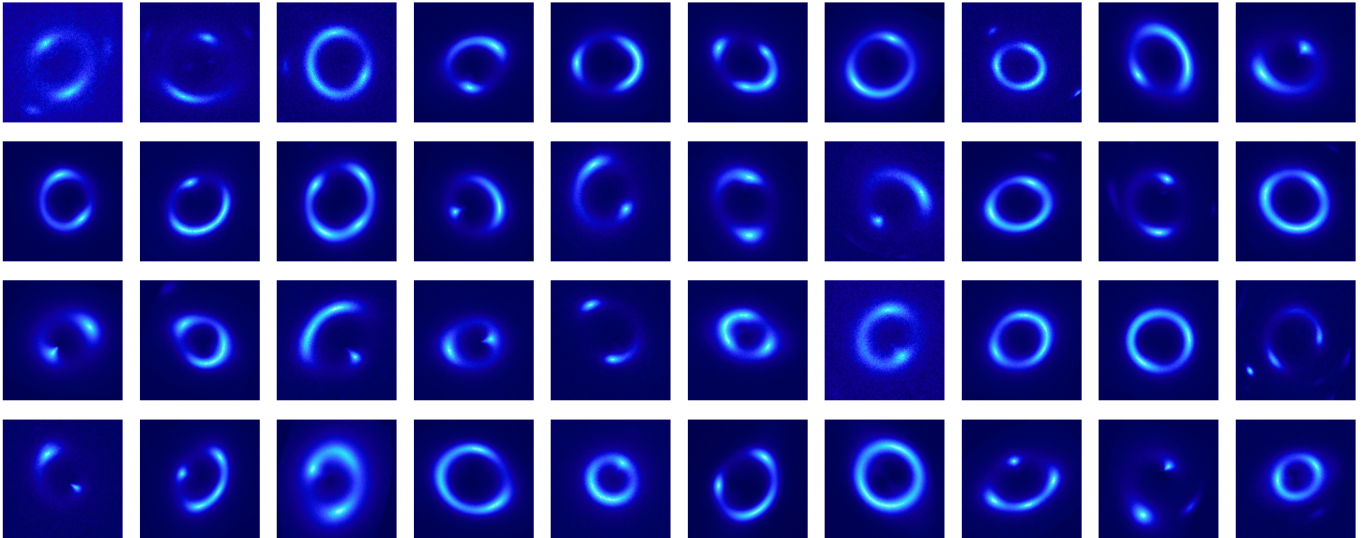


Figure 3. A sample of 40 random strong lenses generated from the training data distribution of the SNPE. The lens systems include a wide variety of closed Einstein rings, doubly imaged sources, and quadruply imaged sources.

test data in experiments with no shear in training data.

Subhalo Profiles: The true profiles of dark matter subhalos are unknown (e.g., Heinze et al. 2024). We explore the effect of changing NFW profiles to truncated NFW profiles and vice versa to quantify the bias introduced in the inferred mass function.

Observational Noise: The distribution of observational noise depends on the instrument, the time and duration of observations, and many other variables. Without introducing non-Gaussianity to the noise, we study the effect of increasing the variance of the noise in the test data.

Although for real data all the listed variations can occur simultaneously, in this case study, we apply one effect at a time to isolate the effects of individual variations. The specific modified parameters to test the NRE and the SNPE frameworks can be found in Table 3 and 4 respectively.

5. RESULTS AND DISCUSSION

5.1. Neural Ratio Estimator

We evaluate the calibrated NRE on lenses that are drawn from the training distribution as well as from distributions with minor variations, following the tests in Section 4 and Table 3. The inferred posteriors from the original and the varied distributions are shown in Figure 4. All images used for the posterior inference were generated with the ground truth parameters set at $f_{\text{sub}} = 0.05$ and $\beta = -0.9$, which are consistent with Λ CDM predictions (e.g., Diemand et al. 2007; Kuhlen et al. 2007; Springel et al. 2008; Hiroshima et al. 2018). The ground truth is denoted by the red star in the posterior predictions. In all experiments, we only modify the distribution of one parameter at a time, with the remaining parameters sampled from the same distribution as the training set (Table 1).

Figure 4 is organized as follows: The left-hand side displays variations in the lens plane and noise levels, while the right-hand side shows variations in the source. The columns correspond to the posteriors inferred by combining 50, 100, and 500 lens systems, each row illustrating the effect of a different test.

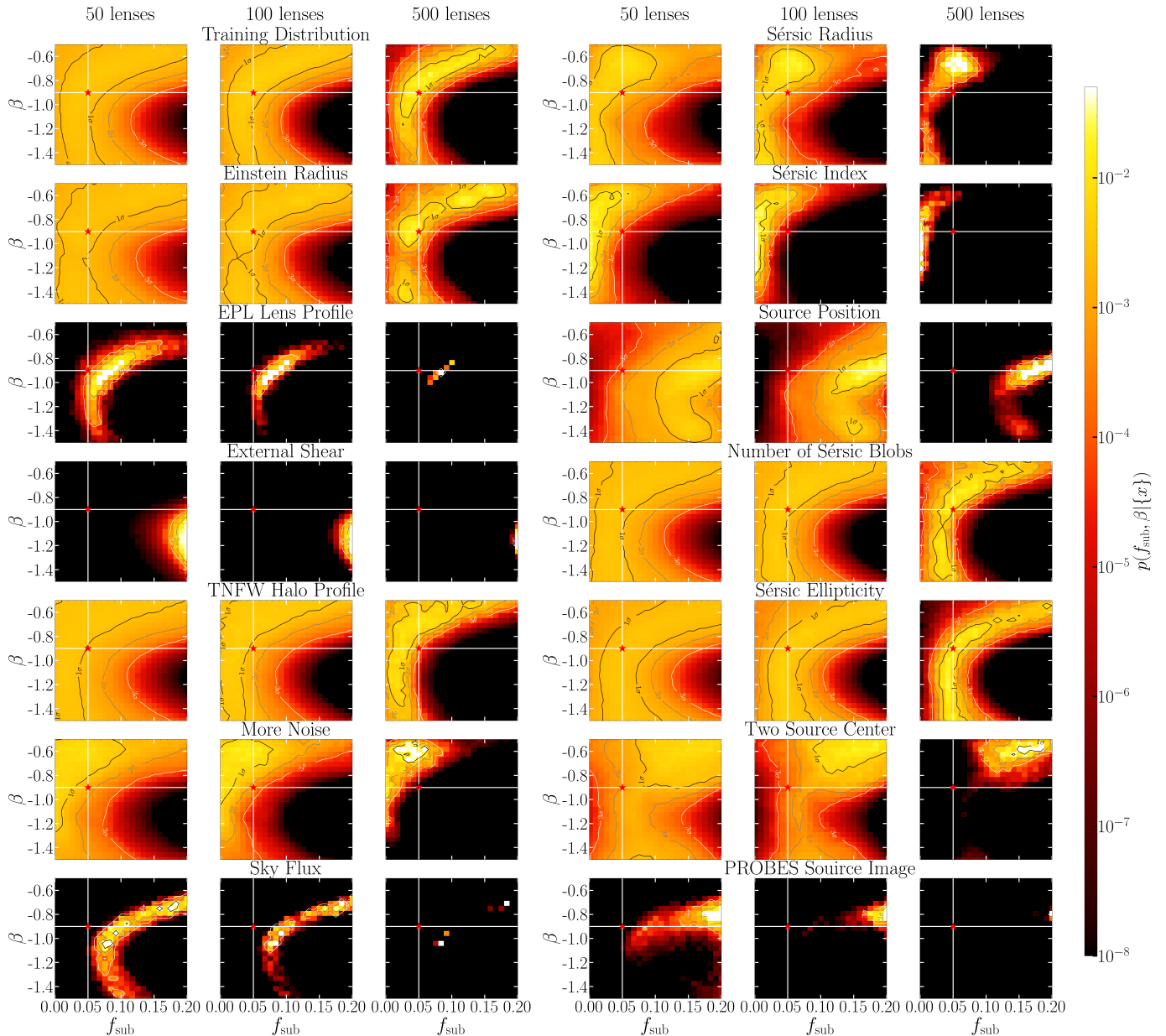


Figure 4. The evaluation of the NRE is conducted on lenses drawn from the training distribution and from distributions with minor variations in the parameters, following Section 4. All evaluation datasets were generated with the ground truth parameters set at $f_{\text{sub}} = 0.05$ and $\beta = -0.9$, which are in accordance with Λ CDM predictions and are marked by a red star. The modifications to the parameter distributions for the individual plots are detailed in Table 3.

The posterior inferred from lenses generated within the training distribution is shown in the top row of the left-hand side. The inferred posterior is unbiased and recovers the ground truth well, indicating that even inference with a large number of lensing systems remains unbiased.

In the second row on the left, we vary the Einstein radius distribution from uniform to a normal distribution with mean $\mu = 1.4$ and standard deviation $\sigma = 0.2$, while maintaining the same boundaries as in the training distribution. While the posteriors for 50 and 100 lenses recover the ground truth, the posterior for 500

Table 3. Parameter distribution variations used to create Figure 4. The modifications are described in more detail in Section 4. Here, $\mathcal{N}(\mu, \sigma)$ represents a normal distribution with mean μ and standard deviation σ , and $\mathcal{U}[a, b]$ denotes a uniform distribution between a and b .

Plot Title	Modified Parameter	New Distribution
Training Distribution	None	
Einstein Radius	Einstein radius θ_E	$\mathcal{N}(1.4, 0.2) \geq 1.0, \leq 1.5$
EPL Lens Profile	Power-law slope of lens γ_{EPL}	$\mathcal{N}(2.0, 0.02)$
External Shear	Added external shear components $\gamma_{1/2}$	$\mathcal{N}(0.0, 0.1)$
TNFW Halo Profile	Truncation of NFW, truncation scale τ	5
More Noise	Noise in the image at 1% of the sky flux	
Sky Flux	Different magnitude of sky background mag_{sky}	21.4
Sérsic Radius	Sérsic radius $R_{\text{sérsic}}$	$\mathcal{N}(0.2, 0.2) \geq 0.05$
Sérsic Index	Sérsic index $n_{\text{sérsic}}$	$\mathcal{N}(5.5, 1.5) \geq 0.8$
Source Position	Source centers $(\hat{x}_{\text{source}}, \hat{y}_{\text{source}})$	$\mathcal{N}(0.05, 0.15)$
Number of Sérsic Blobs	Number of Sérsic blobs in the source N	$\mathcal{U}[40 - 45]$
Sérsic Ellipticity	Source axis ratio $q_{\text{sérsic}}$	$\mathcal{N}(0.75, 0.2) \geq 0.5, \leq 0.99$
Two Source Center	Source position $(\hat{x}_{\text{source1}}, \hat{y}_{\text{source1}}), (\hat{x}_{\text{source2}}, \hat{y}_{\text{source2}})$	$\mathcal{N}_1(0.0, 0.1), \mathcal{N}_2(-0.2, 0.1)$
Probes Dataset as Sources	Analytic Sérsic source profiles to Probes dataset	

systems shows multiple posterior modes. This is an artifact of the distributional shift and causes the posterior to exhibit a bias that is detectable through coverage tests such as TARP (Lemos et al. 2023).

The third row shows the posterior when changing the main deflector model from a SIE to an EPL profile, with the mass slope drawn from a normal distribution with mean $\mu = 2.0$ and standard deviation $\sigma = 0.02$. For a slope of $\gamma_{\text{EPL}} = 2.0$, the EPL profile corresponds to a SIE profile. Despite this minimal variation ($\sim 1\%$), even for 50 lenses the posterior is highly biased, and the ground truth is outside the 3σ region.

In the fourth row, we introduce a small external shear defined by two shear components $\gamma_{1,2}$ each with a mean of $\mu = 0.0$ and standard deviation $\sigma = 0.1$. The shear is highly degenerate with the ellipticity of the lens profile and is typically used to model the local lens environment (e.g., Oguri et al. 2005; Koopmans et al. 2006; Sonnenfeld et al. 2013; Shu et al.

2016, 2017; Talbot et al. 2021). The additional external shear significantly biases the network output, pushing the obtained posterior towards the boundaries of the parameters of interest.

The fifth row introduces a modification to the dark matter halo mass profiles, changing from NFW to truncated NFW profiles with a truncation radius five times the scale radius, converting infinitely extended NFW profiles to finite mass profiles. The resulting posterior exhibits a clear bias.

The sixth row examines the effects of increasing the variance of the observational Gaussian noise by $\sim 1\%$ of the sky flux (the zero point of the image), which significantly biases the networks output. The last row on the left side shows the impact of reducing the image zero point. The posterior is strongly biased, highlighting the sensitivity to variations in sky flux and noise distributions.

The right panels of Figure 4 show the posteriors obtained when modifying the distribution of the background source parameters. Rows one

to six correspond to variations in size, slope, position, complexity (number of Sérsic components), source ellipticity, and number of primary sources behind a deflector. Almost every modification results in a strong bias when combining multiple lenses. However, the strongest bias is observed in the last row, exploring the effect of using real images of galaxies from Stone & Courteau (2019) for testing the model.

These tests reveal that the bias introduced to the posteriors is highly unpredictable. In some cases, shifts in parameters that significantly impact the images, such as the size of the background sources, result in relatively minor biases. Conversely, changes in parameters that are highly degenerate with others, like external shear and ellipticity, can induce substantial biases in the posteriors, even when they cause nearly imperceptible changes in the data.

The initial parameterization used to train the NRE is within the range of usual state-of-the-art parameterization for lens modeling, and the deviations tested here are mostly physically very small and are very likely to occur in a realistic data analysis setting where the ground truth is not available. The effects of the changes in the underlying parameter distributions on the NRE predictions are highly nonlinear and unpredictable, which makes it difficult to trust the inferred posterior with this model. This makes NREs applicable to cases where both, the underlying distribution of parameters and the physical model, are perfectly known (e.g., for sensitivity predictions). For strong lensing specifically and astrophysical data analysis in general, this is very rarely the case.

5.2. Neural Posterior Estimator

By incorporating a hierarchical inference step, which effectively models the prior distribution, the SNPE framework can correct for certain distributional shifts. This allows for accurate inference even with misspecified priors, provided these priors remain within the test distribu-

tion and are low dimensional. We demonstrate this capability by first testing scenarios where the Einstein radii in the test data are sampled from a different distribution, but still within the bounds of the training data.

We then empirically test the robustness of SNPE to data generated outside the bounds of the training data. We do this by considering modifications to the dark matter subhalo profiles (replacing tNFW profiles with NFW profiles) and also changing the distribution of the background source morphologies as detailed in Table 4. For the population-level inference of dark matter model we use ten mock targets for each test.

Figure 5 illustrates the effect of different tests. The red contours show the SNPE results for inference on the training data distribution, while the other colors show the effects of different modifications (Table 4), based on the tests from Section 4.

The target images for the SNPE are generated using the same random seed, ensuring that, between the evaluations on the training distribution and the modifications, only the varied parameter changes. This implies that the specific realization of positions and masses of the subhalos, along with all other unmodified parameters (including the specific realization of observational noise), remain consistent across the ten different evaluated images. The only exception to this is the variation of the Einstein radius, since our parameterization of the abundance of subhalos relies on the lens mass, which is directly correlated to the Einstein radius. We expect that for the inference to be robust against these modifications, the posterior of the dark matter normalization, Σ_{sub} , should remain consistent across the various tests.

It is important to note that the prior on the subhalo abundance for the training distribution, used to generate the training data, is a narrow normal distribution with mean $\mu_{\Sigma} = 0.002$ and

Table 4. Parameter distributions variations used to create Figure 5. The modifications are described in more detail in Section 4. $\mathcal{N}(\mu, \sigma)$ represents a normal distribution with mean μ and standard deviation σ .

	Modified Parameter	New Distribution
Training Distribution	None	
Bigger Einstein Radius	Einstein radius θ_E	$\mathcal{N}(1.5, 0.1)$
Smaller Einstein Radius	Einstein radius θ_E	$\mathcal{N}(0.7, 0.1)$
NFW Halo Profiles	Usage of NFW mass profile for subhalos	
Spiral Source Galaxies	SKIRT TNG dataset as source images	
Added Blobs	Addition of Sérsic light blobs to sources	30-50 Sérsic profiles
AstroCLIP split	Elliptical galaxies are split with AstroCLIP	

standard deviation $\sigma_\Sigma = 0.001$. As seen in Figure 5, this narrow prior limits the range of biases. If the prior is broadened to either a uniform distribution or a normal distribution with a broader standard deviation, the observed biases are expected to increase.

The specific modifications used in each test from Figure 5 are detailed in Table 4. The top left panel in Figure 5 shows the effect of modifying the Einstein radius distribution. The training distribution draws the Einstein radius from a normal distribution with mean $\mu = 1.1$ arcsec and standard deviation $\sigma = 0.15$. The yellow contours show the effect of drawing the Einstein radius from a normal distribution with ($\mu_{\text{small}} = 0.7, \sigma_{\text{small}} = 0.1$), and the blue contours correspond to drawing the Einstein radius from a normal distribution with ($\mu_{\text{big}} = 1.5, \sigma_{\text{big}} = 0.1$). This modification demonstrates that lens systems with larger Einstein radii are more constraining on the dark matter abundance than systems with smaller radii. The results suggest that a modification of the Einstein radius distribution does not bias the inferred posteriors within this framework, but in general, systems with larger Einstein radii are more constraining than systems with smaller Einstein radii.

The second variation, shown in the top right panel of Figure 5, changes the subhalo profiles from truncated NFW profiles to NFW mass profiles. The gray contours show the effect on the

inferred dark matter normalization constant. The bias in the posterior estimation resulting from this minor change suggests that the specific density profile used in training simulations can negatively impact the accuracy of the inference on the mass function parameters. Note that even within Cold Dark Matter cosmologies, there is theoretical uncertainty in the expected profiles of low-mass subhalos (e.g., Heinze et al. 2024).

The next variations, in the bottom left panel, test the effect of background sources that are outside of the training distribution. For the training data, we used elliptical source images from the DESI survey (Dey et al. 2019), selected by Barco et al. (2024). The green contours originate from target images generated using the SKIRT TNG dataset (Bottrell et al. 2024), simulated for the Hyper Suprime-Cam Subaru Strategic Program (Aihara et al. 2018). This dataset contains only spiral galaxies. The strong bias observed highlights that precise knowledge of the source profile is required for unbiased dark matter inference.

Since the difference between spiral and elliptical galaxies is significant, so we also explored the performance of the SNPE network under more subtle source variations, shown on the bottom right panel of Figure 5.

First, we took the original elliptical source galaxy images and added between 30 and 50 small Sérsic light profiles, with a brightness of at

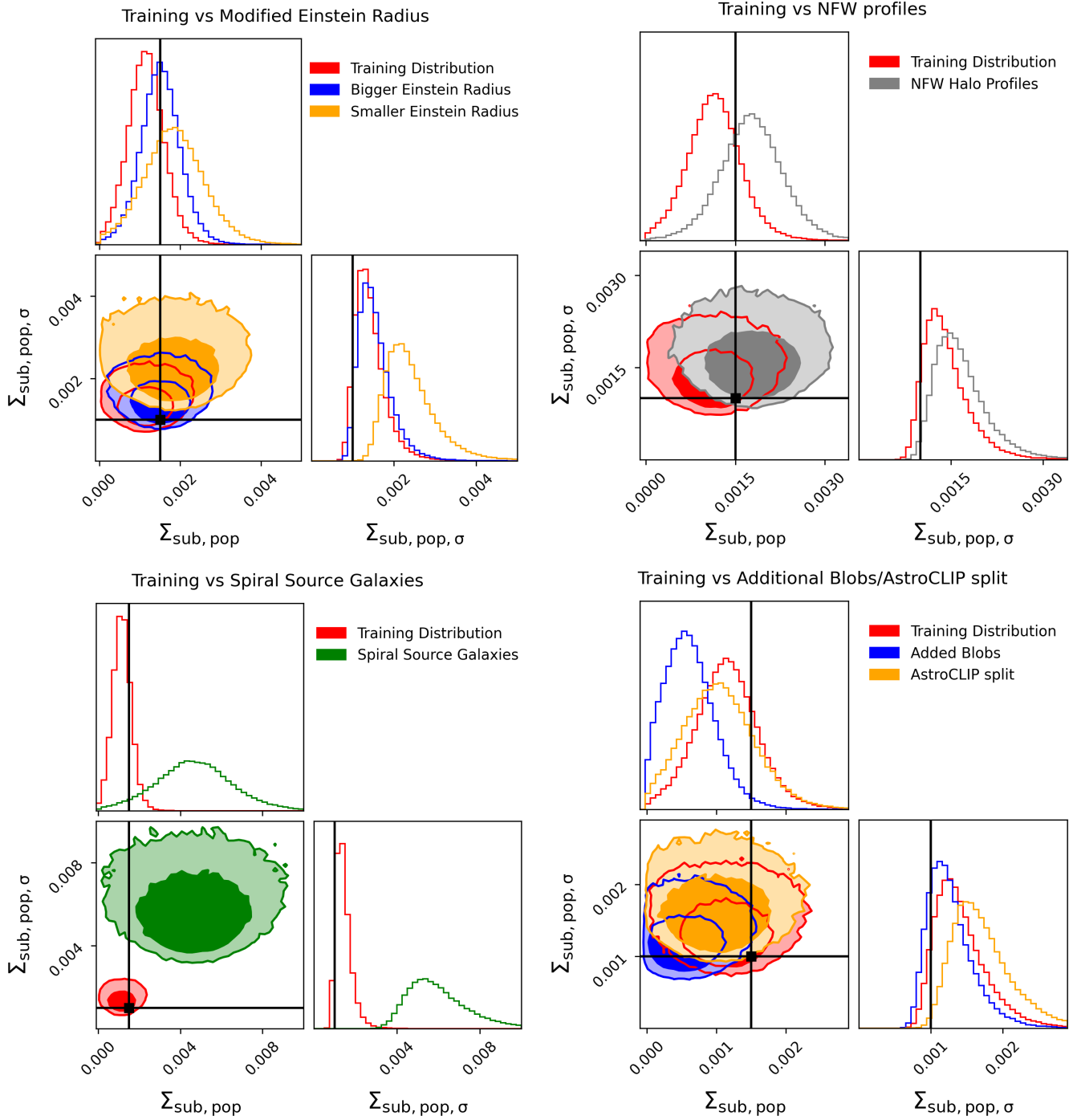


Figure 5. Evaluation of the SNPEs on lenses drawn from the training distribution and on variations in the underlying parameter distributions, following the tests described in Section 4. We modify the Einstein radius distribution, the subhalo mass profile, and the source profiles. Details can be found in Table 4. The red contours always show the SNPE results for inference on the training data distribution.

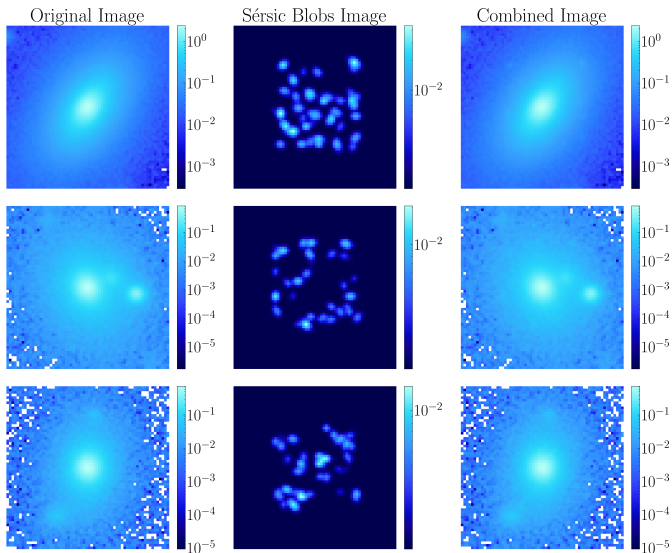


Figure 6. Examples of Sérsic blobs added to the training source image to create OOD data. The differences are barely visible to the eye.

least an order of magnitude less than the main background source galaxy. The bottom right panel of Figure 6 shows examples of these variations. By eye, these changes are barely visible. The effect of these modifications on the SNPE prediction is shown in the blue contours, indicating that the true distribution is now outside the 2σ contours of the posterior on the variational parameters.

As an additional test, we split the elliptical galaxies into two datasets using AstroCLIP (Parker et al. 2024), a foundation model trained on real galaxy images, to embed the dataset into a latent space. We then split the galaxies into two groups using the K-means clustering algorithm implemented in scikit-learn³. Examples from the two groups are shown in Figure 7. The first group is used to generate the target image, and the second group is used for training data generation. Although we observe a shift in the posterior, the bias is less significant compared to the added blob test. We speculate that this

³ <https://scikit-learn.org/stable/modules/clustering.html#k-means>

is due to the fact that this specific clustering of the data is primarily separating the background galaxies based on their size (Figure 7) while the two classes still have similar small scale surface brightness fluctuations, which is known to be a key factor for detecting subhalos (e.g., Hezaveh et al. 2013).

As in the case of the NRE, these tests show that the SNPE framework is prone to specific biases when testing on data with a different distribution compared to the training data, specifically in the high dimensional space of the background sources, which are known to have strong degeneracies with the subhalo parameters (e.g., Hezaveh et al. 2013; Vegetti & Vogelsberger 2014; Vegetti et al. 2023).

6. CONCLUSION

This paper explored the potential impact of distributional shifts in observational data compared to training data for the inference of dark matter mass function parameters from strong gravitational lensing data using two different machine learning frameworks (NRE and SNPE). We found that in both cases, plausible shifts in the test data (e.g. the morphology of the background sources) can negatively impact the posteriors, introducing non-negligible biases.

When faced with out-of-distribution data, the performance of NREs and SNPEs degrades in unpredictable ways, making it difficult to calibrate the posteriors. These tests induce a bias in the predictions of neural networks, similar to those caused by adversarial attacks (e.g., Szegedy et al. 2013). However, note that unlike realization of adversarial attacks, which can be statistically unlikely in real observational settings, these tests are physically motivated and are meant to represent realistic scenarios of distributional shifts.

Nevertheless, note that even despite these challenges, NREs and NPEs remain powerful tools in situations where distributional shifts are

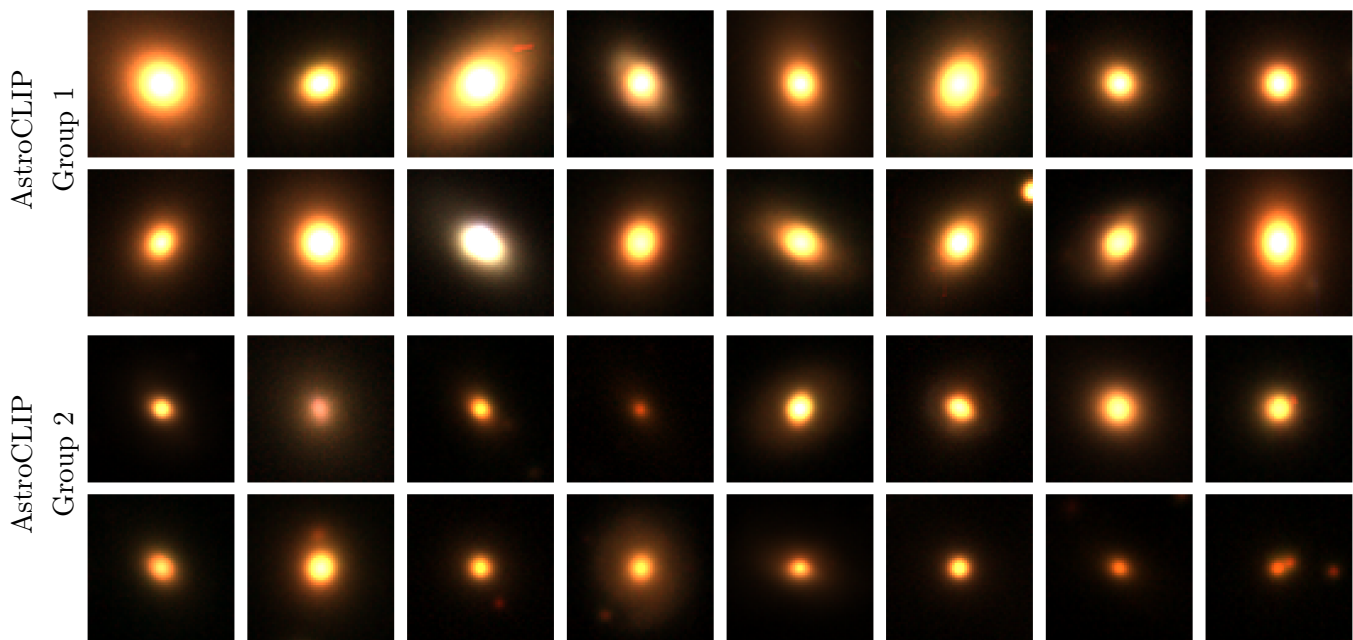


Figure 7. Examples from the two groups of elliptical DESI images grouped using AstroCLIP (Parker et al. 2024). The first group is used to generate the target images, and the second group is used for training data generation.

not a concern, including forecasting and sensitivity analysis based on in-distribution simulations. The challenge of addressing distributional shifts is already a major topic in machine learning (e.g., Masserano et al. 2022; Anau Montel & Weniger 2022; Falkiewicz et al. 2023; Barco et al. 2024; Masserano et al. 2024; Flovik 2024; Wehenkel et al. 2024; Dellaporta et al. 2024) and extensive research in domain adaptation and generalization is being pursued to alleviate these problems. For example, for certain strong lensing analysis frameworks, recently Swierc et al. (2024); Agarwal et al. (2024) have proposed domain adaptation methods to reduce these biases caused by distributional shifts in observational noise.

These tests are also an important lesson beyond the field of strong gravitational lensing, indicating that for inference problems where high accuracy is needed but the true data-generating process is not perfectly known, NRE and SNPE results should be examined with caution. In conclusion, while these frameworks hold great

promise for specific applications, their use with real observational data demands careful consideration of inherent limitations to ensure reliable and unbiased scientific discoveries.

ACKNOWLEDGMENTS

This work is partially supported by Schmidt Futures, a philanthropic initiative founded by Eric and Wendy Schmidt as part of the Virtual Institute for Astrophysics (VIA). The work is in part supported by computational resources provided by Calcul Quebec and the Digital Research Alliance of Canada. Y.H. and L.P. acknowledge support from the Canada Research Chairs Program, the National Sciences and Engineering Council of Canada through grants RGPIN-2020-05073 and 05102, and the Fonds de recherche du Québec through grants 2022-NC-301305 and 300397. A.F. acknowledges the support from the Bourse J. Armand Bombardier.

REFERENCES

- Agarwal, S., Čiprijanović, A., & Nord, B. D. 2024, arXiv e-prints, arXiv:2411.03334. <https://arxiv.org/abs/2411.03334>
- Aihara, H., Arimoto, N., Armstrong, R., et al. 2018, PASJ, 70, S4, doi: [10.1093/pasj/psx066](https://doi.org/10.1093/pasj/psx066)
- Anau Montel, N., & Weniger, C. 2022, arXiv e-prints, arXiv:2211.04291, doi: [10.48550/arXiv.2211.04291](https://doi.org/10.48550/arXiv.2211.04291)
- Baldi, P., Cranmer, K., Faucett, T., Sadowski, P., & Whiteson, D. 2016, European Physical Journal C, 76, 235, doi: [10.1140/epjc/s10052-016-4099-4](https://doi.org/10.1140/epjc/s10052-016-4099-4)
- Barco, G. M., Adam, A., Stone, C., Hezaveh, Y., & Perreault-Levasseur, L. 2024, arXiv e-prints, arXiv:2407.17667, doi: [10.48550/arXiv.2407.17667](https://doi.org/10.48550/arXiv.2407.17667)
- Bertone, G., Hooper, D., & Silk, J. 2005, PhR, 405, 279, doi: [10.1016/j.physrep.2004.08.031](https://doi.org/10.1016/j.physrep.2004.08.031)
- Birrer, S., & Amara, A. 2018, Physics of the Dark Universe, 22, 189, doi: [10.1016/j.dark.2018.11.002](https://doi.org/10.1016/j.dark.2018.11.002)
- Birrer, S., Amara, A., & Refregier, A. 2017, JCAP, 2017, 037, doi: [10.1088/1475-7516/2017/05/037](https://doi.org/10.1088/1475-7516/2017/05/037)
- Birrer, S., Shajib, A. J., Gilman, D., et al. 2021, Journal of Open Source Software, 6, 3283, doi: [10.21105/joss.03283](https://doi.org/10.21105/joss.03283)
- Blumenthal, G. R., Faber, S. M., Primack, J. R., & Rees, M. J. 1984, Nature, 311, 517, doi: [10.1038/311517a0](https://doi.org/10.1038/311517a0)
- Bottrell, C., Yesuf, H. M., Popping, G., et al. 2024, MNRAS, 527, 6506, doi: [10.1093/mnras/stad2971](https://doi.org/10.1093/mnras/stad2971)
- Brehmer, J., Cranmer, K., Louppe, G., & Pavez, J. 2018, Constraining Effective Field Theories with Machine Learning. <https://arxiv.org/abs/1805.00013>
- Brehmer, J., Kling, F., Espejo, I., & Cranmer, K. 2020, Computing and Software for Big Science, 4, 3, doi: [10.1007/s41781-020-0035-2](https://doi.org/10.1007/s41781-020-0035-2)
- Brehmer, J., Louppe, G., Pavez, J., & Cranmer, K. 2018, arXiv e-prints, arXiv:1805.12244, doi: [10.48550/arXiv.1805.12244](https://doi.org/10.48550/arXiv.1805.12244)
- Brehmer, J., Mishra-Sharma, S., Hermans, J., Louppe, G., & Cranmer, K. 2019, ApJ, 886, 49, doi: [10.3847/1538-4357/ab4c41](https://doi.org/10.3847/1538-4357/ab4c41)
- Brennan, S., Benson, A. J., Cyr-Racine, F.-Y., et al. 2019, MNRAS, 488, 5085, doi: [10.1093/mnras/stz1607](https://doi.org/10.1093/mnras/stz1607)
- Collett, T. E., & Cunningham, S. D. 2016, MNRAS, 462, 3255, doi: [10.1093/mnras/stw1856](https://doi.org/10.1093/mnras/stw1856)
- Coogan, A., Montel, N. A., Karchev, K., et al. 2022, One never walks alone: the effect of the perturber population on subhalo measurements in strong gravitational lenses. <https://arxiv.org/abs/2209.09918>
- Cranmer, K., Pavez, J., & Louppe, G. 2015, arXiv e-prints, arXiv:1506.02169, doi: [10.48550/arXiv.1506.02169](https://doi.org/10.48550/arXiv.1506.02169)
- Cyr-Racine, F.-Y., Sigurdson, K., Zavala, J., et al. 2016, PhRvD, 93, 123527, doi: [10.1103/PhysRevD.93.123527](https://doi.org/10.1103/PhysRevD.93.123527)
- Davis, M., Efstathiou, G., Frenk, C. S., & White, S. D. M. 1985, ApJ, 292, 371, doi: [10.1086/163168](https://doi.org/10.1086/163168)
- Dellaporta, C., O'Hara, P., & Damoulas, T. 2024, arXiv e-prints, arXiv:2409.03492, doi: [10.48550/arXiv.2409.03492](https://doi.org/10.48550/arXiv.2409.03492)
- Despali, G., Lovell, M., Vegetti, S., Crain, R. A., & Oppenheimer, B. D. 2020, MNRAS, 491, 1295, doi: [10.1093/mnras/stz3068](https://doi.org/10.1093/mnras/stz3068)
- Dey, A., Schlegel, D. J., Lang, D., et al. 2019, AJ, 157, 168, doi: [10.3847/1538-3881/ab089d](https://doi.org/10.3847/1538-3881/ab089d)
- Diemand, J., Kuhlen, M., & Madau, P. 2007, ApJ, 667, 859, doi: [10.1086/520573](https://doi.org/10.1086/520573)
- Drlica-Wagner, A., Mao, Y.-Y., Adhikari, S., et al. 2019, arXiv e-prints, arXiv:1902.01055, doi: [10.48550/arXiv.1902.01055](https://doi.org/10.48550/arXiv.1902.01055)
- Falkiewicz, M., Takeishi, N., Shekhzadeh, I., et al. 2023, arXiv e-prints, arXiv:2310.13402, doi: [10.48550/arXiv.2310.13402](https://doi.org/10.48550/arXiv.2310.13402)
- Flovik, V. 2024, arXiv e-prints, arXiv:2405.01978, doi: [10.48550/arXiv.2405.01978](https://doi.org/10.48550/arXiv.2405.01978)
- Foreman-Mackey, D., Hogg, D. W., Lang, D., & Goodman, J. 2013, PASP, 125, 306, doi: [10.1086/670067](https://doi.org/10.1086/670067)
- He, K., Zhang, X., Ren, S., & Sun, J. 2016, in 2016 IEEE Conference on Computer Vision and Pattern Recognition (CVPR), 770–778, doi: [10.1109/CVPR.2016.90](https://doi.org/10.1109/CVPR.2016.90)
- Heinze, F. M., Despali, G., & Klessen, R. S. 2024, MNRAS, 527, 11996, doi: [10.1093/mnras/stad3894](https://doi.org/10.1093/mnras/stad3894)

- Hezaveh, Y., Dalal, N., Holder, G., et al. 2016a, JCAP, 2016, 048, doi: [10.1088/1475-7516/2016/11/048](https://doi.org/10.1088/1475-7516/2016/11/048)
- . 2013, ApJ, 767, 9, doi: [10.1088/0004-637X/767/1/9](https://doi.org/10.1088/0004-637X/767/1/9)
- Hezaveh, Y. D., Marrone, D. P., & Holder, G. P. 2012, ApJ, 761, 20, doi: [10.1088/0004-637X/761/1/20](https://doi.org/10.1088/0004-637X/761/1/20)
- Hezaveh, Y. D., Dalal, N., Marrone, D. P., et al. 2016b, ApJ, 823, 37, doi: [10.3847/0004-637X/823/1/37](https://doi.org/10.3847/0004-637X/823/1/37)
- Hinshaw, G., Larson, D., Komatsu, E., et al. 2013, ApJS, 208, 19, doi: [10.1088/0067-0049/208/2/19](https://doi.org/10.1088/0067-0049/208/2/19)
- Hiroshima, N., Ando, S., & Ishiyama, T. 2018, PhRvD, 97, 123002, doi: [10.1103/PhysRevD.97.123002](https://doi.org/10.1103/PhysRevD.97.123002)
- Ivezić, Ž., Kahn, S. M., Tyson, J. A., et al. 2019, ApJ, 873, 111, doi: [10.3847/1538-4357/ab042c](https://doi.org/10.3847/1538-4357/ab042c)
- Karcev, K., Trotta, R., & Weniger, C. 2023, MNRAS, 520, 1056, doi: [10.1093/mnras/stac3785](https://doi.org/10.1093/mnras/stac3785)
- Koopmans, L. V. E., Treu, T., Bolton, A. S., Burles, S., & Moustakas, L. A. 2006, ApJ, 649, 599, doi: [10.1086/505696](https://doi.org/10.1086/505696)
- Kravtsov, A. V., & Borgani, S. 2012, ARA&A, 50, 353, doi: [10.1146/annurev-astro-081811-125502](https://doi.org/10.1146/annurev-astro-081811-125502)
- Kuhlen, M., Diemand, J., & Madau, P. 2007, ApJ, 671, 1135, doi: [10.1086/522878](https://doi.org/10.1086/522878)
- Kuhlen, M., Vogelsberger, M., & Angulo, R. 2012, Physics of the Dark Universe, 1, 50, doi: [10.1016/j.dark.2012.10.002](https://doi.org/10.1016/j.dark.2012.10.002)
- Lemos, P., Coogan, A., Hezaveh, Y., & Perreault-Levasseur, L. 2023, 40th International Conference on Machine Learning, 202, 19256, doi: [10.48550/arXiv.2302.03026](https://doi.org/10.48550/arXiv.2302.03026)
- Mandelbaum, R., van de Ven, G., & Keeton, C. R. 2009, MNRAS, 398, 635, doi: [10.1111/j.1365-2966.2009.15166.x](https://doi.org/10.1111/j.1365-2966.2009.15166.x)
- Masserano, L., Dorigo, T., Izbicki, R., Kuusela, M., & Lee, A. B. 2022, arXiv e-prints, arXiv:2205.15680, doi: [10.48550/arXiv.2205.15680](https://doi.org/10.48550/arXiv.2205.15680)
- Masserano, L., Shen, A., Doro, M., et al. 2024, arXiv e-prints, arXiv:2402.05330, doi: [10.48550/arXiv.2402.05330](https://doi.org/10.48550/arXiv.2402.05330)
- Mishra-Sharma, S. 2022, Machine Learning: Science and Technology, 3, 01LT03, doi: [10.1088/2632-2153/ac494a](https://doi.org/10.1088/2632-2153/ac494a)
- Navarro, J. F., Frenk, C. S., & White, S. D. M. 1997, ApJ, 490, 493, doi: [10.1086/304888](https://doi.org/10.1086/304888)
- Oguri, M., Keeton, C. R., & Dalal, N. 2005, MNRAS, 364, 1451, doi: [10.1111/j.1365-2966.2005.09697.x](https://doi.org/10.1111/j.1365-2966.2005.09697.x)
- Papamakarios, G., & Murray, I. 2016, arXiv e-prints, arXiv:1605.06376, doi: [10.48550/arXiv.1605.06376](https://doi.org/10.48550/arXiv.1605.06376)
- Parker, L., Lanusse, F., Golkar, S., et al. 2024, Monthly Notices of the Royal Astronomical Society, 531, 4990–5011, doi: [10.1093/mnras/stae1450](https://doi.org/10.1093/mnras/stae1450)
- Planck Collaboration, Aghanim, N., Akrami, Y., et al. 2020, A&A, 641, A6, doi: [10.1051/0004-6361/201833910](https://doi.org/10.1051/0004-6361/201833910)
- Rozet, F., Andry, G., Lanusse, F., & Louppe, G. 2024, arXiv e-prints, arXiv:2405.13712, doi: [10.48550/arXiv.2405.13712](https://doi.org/10.48550/arXiv.2405.13712)
- Schneider, P., & Sluse, D. 2014, A&A, 564, A103, doi: [10.1051/0004-6361/201322106](https://doi.org/10.1051/0004-6361/201322106)
- Sérsic, J. L. 1963, Boletín de la Asociación Argentina de Astronomía La Plata Argentina, 6, 41
- Shu, Y., Bolton, A. S., Mao, S., et al. 2016, ApJ, 833, 264, doi: [10.3847/1538-4357/833/2/264](https://doi.org/10.3847/1538-4357/833/2/264)
- Shu, Y., Brownstein, J. R., Bolton, A. S., et al. 2017, ApJ, 851, 48, doi: [10.3847/1538-4357/aa9794](https://doi.org/10.3847/1538-4357/aa9794)
- Sonnenfeld, A., Li, S.-S., Despali, G., et al. 2023, A&A, 678, A4, doi: [10.1051/0004-6361/202346026](https://doi.org/10.1051/0004-6361/202346026)
- Sonnenfeld, A., Treu, T., Gavazzi, R., et al. 2013, ApJ, 777, 98, doi: [10.1088/0004-637X/777/2/98](https://doi.org/10.1088/0004-637X/777/2/98)
- Springel, V., Wang, J., Vogelsberger, M., et al. 2008, MNRAS, 391, 1685, doi: [10.1111/j.1365-2966.2008.14066.x](https://doi.org/10.1111/j.1365-2966.2008.14066.x)
- Stone, C., & Courteau, S. 2019, ApJ, 882, 6, doi: [10.3847/1538-4357/ab3126](https://doi.org/10.3847/1538-4357/ab3126)
- Stone, C., Adam, A., Coogan, A., et al. 2024, arXiv e-prints, arXiv:2406.15542, doi: [10.48550/arXiv.2406.15542](https://doi.org/10.48550/arXiv.2406.15542)
- Swierc, P., Tamargo-Arizmendi, M., Čiprijanović, A., & Nord, B. D. 2024, arXiv e-prints, arXiv:2410.16347, doi: [10.48550/arXiv.2410.16347](https://doi.org/10.48550/arXiv.2410.16347)
- Szegedy, C., Zaremba, W., Sutskever, I., et al. 2013, arXiv e-prints, arXiv:1312.6199, doi: [10.48550/arXiv.1312.6199](https://doi.org/10.48550/arXiv.1312.6199)

- Talbot, M. S., Brownstein, J. R., Dawson, K. S., Kneib, J.-P., & Bautista, J. 2021, *MNRAS*, 502, 4617, doi: [10.1093/mnras/stab267](https://doi.org/10.1093/mnras/stab267)
- Tessore, N., & Metcalf, R. B. 2015, *A&A*, 580, A79, doi: [10.1051/0004-6361/201526773](https://doi.org/10.1051/0004-6361/201526773)
- Treu, T., Gavazzi, R., Gorecki, A., et al. 2009, *ApJ*, 690, 670, doi: [10.1088/0004-637X/690/1/670](https://doi.org/10.1088/0004-637X/690/1/670)
- Vegetti, S., Koopmans, L. V. E., Bolton, A., Treu, T., & Gavazzi, R. 2010, *MNRAS*, 408, 1969, doi: [10.1111/j.1365-2966.2010.16865.x](https://doi.org/10.1111/j.1365-2966.2010.16865.x)
- Vegetti, S., & Vogelsberger, M. 2014, *MNRAS*, 442, 3598, doi: [10.1093/mnras/stu1284](https://doi.org/10.1093/mnras/stu1284)
- Vegetti, S., Birrer, S., Despali, G., et al. 2023, arXiv e-prints, arXiv:2306.11781, doi: [10.48550/arXiv.2306.11781](https://doi.org/10.48550/arXiv.2306.11781)
- Wagner-Carena, S., Aalbers, J., Birrer, S., et al. 2023, *ApJ*, 942, 75, doi: [10.3847/1538-4357/aca525](https://doi.org/10.3847/1538-4357/aca525)
- Wagner-Carena, S., Lee, J., Pennington, J., et al. 2024, arXiv e-prints, arXiv:2404.14487, doi: [10.48550/arXiv.2404.14487](https://doi.org/10.48550/arXiv.2404.14487)
- Wagner-Carena, S., Park, J. W., Birrer, S., et al. 2021, *ApJ*, 909, 187, doi: [10.3847/1538-4357/abdf59](https://doi.org/10.3847/1538-4357/abdf59)
- Wehenkel, A., Gamella, J. L., Sener, O., et al. 2024, arXiv e-prints, arXiv:2405.08719, doi: [10.48550/arXiv.2405.08719](https://doi.org/10.48550/arXiv.2405.08719)
- White, S. D. M., Frenk, C. S., Davis, M., & Efstathiou, G. 1987, *ApJ*, 313, 505, doi: [10.1086/164990](https://doi.org/10.1086/164990)
- Zhang, G., Şengül, A. Ç., & Dvorkin, C. 2024, *MNRAS*, 527, 4183, doi: [10.1093/mnras/stad3521](https://doi.org/10.1093/mnras/stad3521)
- Zhang, G., Mishra-Sharma, S., & Dvorkin, C. 2022, *MNRAS*, 517, 4317, doi: [10.1093/mnras/stac3014](https://doi.org/10.1093/mnras/stac3014)